Modeling ring current ion and electron dynamics and plasma instabilities during a high-speed stream driven storm

V. K. Jordanova,[1] D. T. Welling,[1,2] S. G. Zaharia,[1] L. Chen,[3] and R. M. Thorne[3]

[1] The temporal and spatial development of the ring current is evaluated during the 23–26 October 2002 high-speed stream (HSS) storm, using a kinetic ring current-atmosphere interactions model with self-consistent magnetic field (RAM-SCB). The effects of nondipolar magnetic field configuration are investigated on both ring current ion and electron dynamics. As the self-consistent magnetic field is depressed at large ($>4R_E$) radial distances on the nightside during the storm main phase, the particles' drift velocities increase, the ion and electron fluxes are reduced and the ring current is confined closer to Earth. In contrast to ions, the electron fluxes increase closer to Earth and the fractional electron energy reaches $\sim$20% near storm peak due to better electron trapping in a nondipolar magnetic field. The ring current contribution to *Dst* calculated using Biot-Savart integration differs little from the DPS relation except during quiet time. RAM-SCB simulations underestimate |SYM-H| minimum by $\sim$25% but reproduce very well the storm recovery phase. Increased anisotropies develop in the ion and electron velocity distributions in a self-consistent magnetic field due to energy dependent drifts, losses, and dispersed injections. There is sufficient free energy to excite whistler mode chorus, electromagnetic ion cyclotron (EMIC), and magnetosonic waves in the equatorial magnetosphere. The linear growth rate of whistler mode chorus intensifies in the postmidnight to noon sector, EMIC waves are predominantly excited in the afternoon to midnight sector, and magnetosonic waves are excited over a broad MLT range both inside and outside the plasmasphere. The wave growth rates in a dipolar magnetic field have significantly smaller magnitude and spatial extent.

1. Introduction

[2] High speed solar wind streams (HSS) emanate from coronal holes, dark regions in the corona where the magnetic field is open, and stream into interplanetary space [*Krieger et al.*, 1973]. These streams overtake slower speed streams ahead of them and form corotating interaction regions (CIR) causing recurrent geomagnetic activity at Earth [*Sheeley et al.*, 1976; *Tsurutani et al.*, 1995]. The resulting magnetic storms have typically weak to moderate intensity due to the highly oscillating B_z component of the Alfvén waves occurring within the HSS, and consequently

[1]Los Alamos National Laboratory, Los Alamos, New Mexico, USA.
[2]Atmospheric, Oceanic, and Space Sciences Department, University of Michigan, Ann Arbor, Michigan, USA.
[3]Department of Atmospheric and Oceanic Science, University of California, Los Angeles, California, USA.

Corresponding author: V. K. Jordanova, Los Alamos National Laboratory, PO Box 1663, MS D466, Los Alamos, NM 87545, USA. (vania@lanl.gov)

HSS-driven storms have not received much attention in the past. However, because of the extended period of geomagnetic activity persisting for several days, it has been argued that the energy input to the magnetosphere/atmosphere during HSS is comparable to the energy input during coronal mass ejections (CME) [*Kozyra et al.*, 2006; *Turner et al.*, 2006]. In addition, HSS produce storm levels of enhanced convection, relativistic electron energization, and particle precipitation [*Meredith et al.*, 2011], therefore HSS are important drivers of magnetospheric activity and the response at Earth during their passage requires further investigation.

[3] HSS storms are particularly effective in producing relativistic electrons during the storm recovery phases [e.g., *Paulikas and Blake*, 1979; *Miyoshi and Kataoka*, 2008] and are an increased threat to spacecraft systems [e.g., *Wrenn*, 2009]. It is important to establish the principal acceleration and loss processes in the Earth's radiation belts operating during HSS since the observed fluxes are a net result of them. Proposed radiation belt heating mechanisms that are being debated are acceleration by ultralow frequency (ULF) wave enhanced radial diffusion [e.g., *Li et al.*, 2001; *Elkington et al.*, 2003] or local heating of $\sim$100 keV ring

current electrons to MeV energies by very low frequency (VLF) chorus [e.g., *Horne and Thorne*, 1998; *Summers et al.*, 1998]. Another type of waves, known as fast magnetosonic waves, can also be effective in accelerating electrons from ~10 keV up to relativistic energies in the outer radiation belts [e.g., *Horne et al.*, 2007]. Suggested dominant loss processes for the radiation belts are scattering by VLF chorus just outside the plasmapause [e.g., *Lorentzen et al.*, 2001; *Thorne et al.*, 2005], and resonance with electromagnetic ion cyclotron (EMIC) waves [e.g., *Thorne and Kennel*, 1971; *Thorne et al.*, 2006; *Jordanova et al.*, 2008]. These plasma waves have been observed in the magnetosphere with different intensities, spatial distributions, and occurrence rates. Whistler mode chorus emissions are enhanced during active geomagnetic conditions and are usually observed outside the plasmasphere over a broad magnetic local time (MLT) range with peak storm time amplitudes in the range of 30–100 pT. Nightside chorus is strongest in the premidnight to dawn region between $3R_E$ and $7R_E$, while dayside chorus intensifies at distances larger than $3R_E$ in the dawn to prenoon MLT region [*Meredith et al.*, 2001; *Santolík and Gurnett*, 2003; *Li et al.*, 2009]. These VLF emissions are considered to be initially excited by cyclotron resonance with a highly anisotropic distribution of energetic (~10 keV) electrons [e.g., *Kennel and Thorne*, 1967; *Li et al.*, 2009, 2010], followed by nonlinear evolution into discrete chorus elements [*Nunn et al.*, 2003; *Omura et al.*, 2008]. Ray-tracing modeling studies of chorus waves have shown that these emissions may propagate into the plasmasphere and evolve into plasmaspheric hiss [e.g., *Bortnik et al.*, 2008]. On the other hand, EMIC waves are excited by anisotropic distributions of energetic ring current ions [e.g., *Mauk and McPherron*, 1980; *Horne and Thorne*, 1993, 1997; *Jordanova et al.*, 1997, 2001]. EMIC waves are enhanced during geomagnetic storms with the most intense emissions confined to the dusk MLT region [*Erlandson and Ukhorskiy*, 2001; *Meredith et al.*, 2003]. Theoretical studies suggest that the equatorial region is favored for EMIC wave generation. This is supported by CRRES observations that show a source region within $\pm 11°$ of the equator [*Loto'aniu et al.*, 2005] and by the absence of reflected wave packet energy [*Fraser et al.*, 1996; *Mursula*, 2007]. Finally, fast magnetosonic waves, also called equatorial noise, are associated with ring-type (in the direction perpendicular to the magnetic field) proton velocity distributions [e.g., *Perraut et al.*, 1982; *Horne et al.*, 2000] at energies of the order of ~10 keV. This was recently confirmed by linear dispersion theory [*Chen et al.*, 2010b] and particle-in-cell simulations [*Liu et al.*, 2011]. Magnetosonic waves occur at frequencies between the proton gyrofrequency and the lower hybrid frequency, and are primarily confined within several degrees of the geomagnetic equator both inside and outside the plasmapause [e.g., *Russell et al.*, 1970; *Santolík et al.*, 2002].

[4] Ring current electrons are the seed population that gets accelerated to form the radiation belts. Their dynamics, however, have been overlooked in the past as most of the ring current energy density is carried by ions [*Daglis et al.*, 1999]. Initial observations of low-energy (<50 keV) electron and proton fluxes from the OGO 3 satellite indicated that the electron component may provide about 25% of the ring current energy during storm times [*Frank*, 1967]. More recently, *Liu et al.* [2005] analyzed Explorer 45 data,

spanning larger energy (1–200 keV) and spatial range ($2–5R_E$), around minimum $Dst = -171$ nT of the 17 December 1971 storm. They found that ring current electrons may contribute ~7.5% of the ring current energy over this spatial range during quiet time; the electron contribution may increase to 19% during storm time. An initial simulation of *Jordanova and Miyoshi* [2005] using an analytical Volland-Stern electric field and a dipolar magnetic field showed that the electron contribution during the large storm of 21 October 2001 was about 2% during quiet time and about 10% near peak $Dst = -187$ nT. The dynamics of ring current electrons during the 19 October 1998 storm (min $Dst = -112$ nT) in nondipolar magnetic field geometry were studied by *Chen et al.* [2006]. Tracing equatorially mirroring protons and electrons and solving the force-balance equation in the equatorial plane they found that the ring current intensity and subsequent contribution to Dst is reduced by about 25% by making the simulation magnetically self-consistent. Similar reduction was obtained by *Jordanova et al.* [2006, 2010b] and *Zaharia et al.* [2006] studying ring current proton development in a three-dimensional (3-D) magnetically self-consistent simulation.

[5] In the present paper we investigate ring current development during the HSS-driven storm of 23–26 October 2002 using our newly developed ring current-atmosphere interactions model with self-consistent magnetic field (RAM-SCB). This time period is one of the rare HSS passages at Earth that triggered significant geomagnetic activity – a magnetic storm with minimum $Dst \approx -100$ nT. In addition to ring current ion dynamics simulated in previous studies [*Jordanova et al.*, 2009, 2010b; *Zaharia et al.*, 2010; *Welling et al.*, 2011], we have extended RAM-SCB to include the dynamics of ring current electrons and we investigate their evolution during the HSS-driven storm. An important feature of RAM-SCB is that it resolves the full storm time pressure anisotropy, which is crucial for the excitation of plasma waves in the inner magnetosphere. In this study, we simulate the generation of whistler mode chorus, EMIC and magnetosonic waves, which are important for the acceleration and loss of radiation belt electrons. We address two outstanding questions related to HSS-geospace coupling: (1) What is the temporal and spatial evolution of ring current ion and electron fluxes, and (2) which magnetospheric plasma waves are excited by these populations during the HSS passage at Earth?

2. Observations

[6] Interplanetary data from the Advanced Composition Explorer (ACE) during the storm interval under investigation are shown in Figure 1. The measurements of solar wind plasma from the SWEPAM instrument indicate a stream-stream interaction between hours ~30 and 36, where a fast stream of ~700 km/s overtakes a slower stream of ~400 km/s speed. Measurements of the interplanetary magnetic field (IMF) from the MFI instrument are shown in Figures 1c and 1d, and the interplanetary electric field (IEF) as defined in *Hairston et al.* [2003] is plotted in Figure 1e. Ahead of the HSS interface the solar wind proton density and IMF are enhanced, causing the initial phase of the magnetic storm. The driving of the magnetosphere during the passage of the interaction region is mainly through the large negative B_z excursions, attaining peak values $B_z \approx -15$ nT at the leading
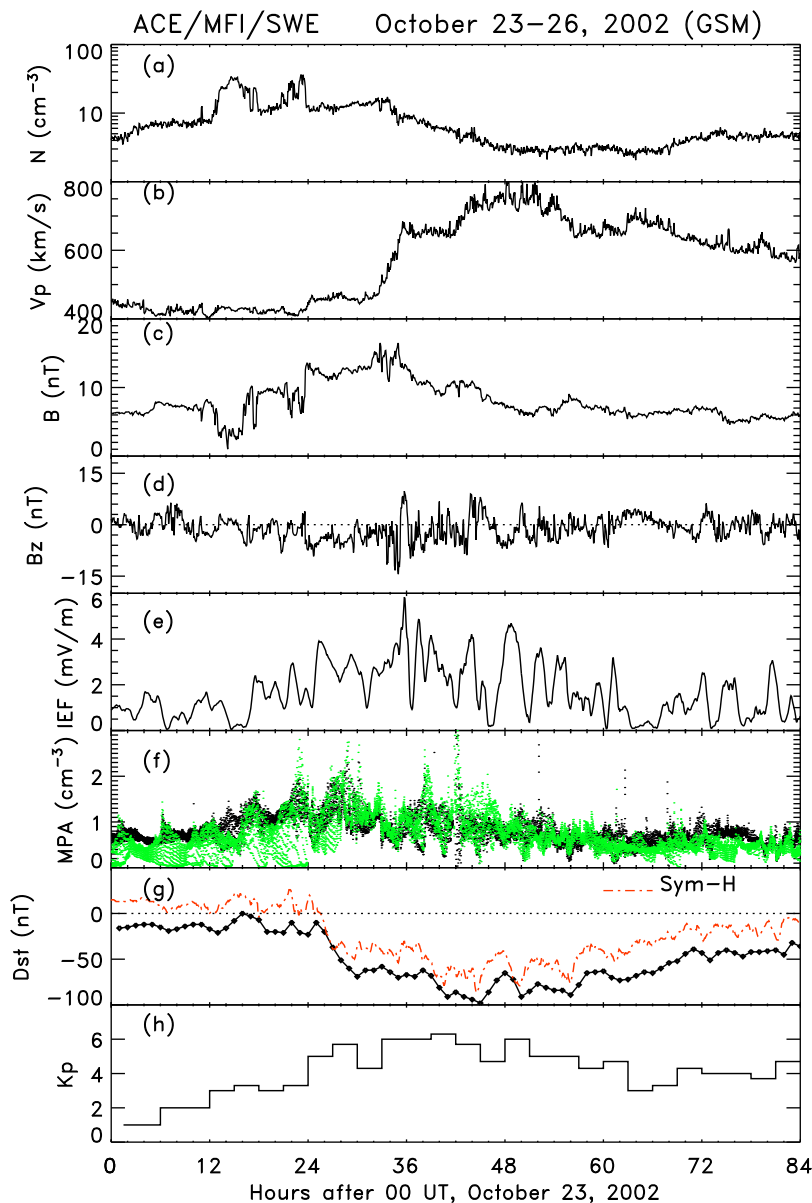
Figure 1. Interplanetary data from ACE during 23–26 October 2002. (a) Proton density, (b) solar wind speed, (c) magnetic field strength, (d) B_z (GSM) component of the magnetic field, and (e) interplanetary electric field. (f) Nightside plasma sheet ion (black) and electron (green) density from geosynchronous LANL satellites. (g) Measured *Dst* (diamond) and SYM-H (dash-dotted) indices, and (h) the *Kp* index.

edge of the HSS. The IEF is highly fluctuating but remains enhanced above ∼2 mV/m in the vicinity of and following the stream interface; the maximum IEF of ∼6 mV/m is reached at hour ∼36. A long train of Alfvénic fluctuations with peak-to-peak IMF B_z amplitude of ∼5 nT occurred in the high speed flow behind the HSS interaction.

[7] Figure 1f displays data from the Magnetospheric Plasma Analyzer (MPA) along the nightside geosynchronous orbit (between MLT = 18 and MLT = 6) from all LANL satellites available during the investigated period. Plotted are the plasma sheet ion and electron densities integrated in the energy range of ∼100 eV to 40 keV. The data show high variability throughout the interval with enhancements reaching ≤2 cm^{-3} during the storm main phase on

24 October, thus there is no superdense plasma sheet [*Borovsky et al.*, 1997] that is usually observed during large storms. The plasma sheet density was reduced to ∼0.5 cm^{-3} during the recovery phase of the storm on 25 October.

[8] The geomagnetic disturbance indices provided by the World Data Center at Kyoto, Japan, with 1-hour resolution (*Dst*) and 1-min resolution (SYM-H) are plotted in Figure 1g. The passage at Earth of the HSS interaction region caused a moderate magnetic storm with a step-like *Dst* profile and minimum *Dst* = −98 nT at hour = 45 (minimum SYM-H = −88 nT at hour ∼44.5). The 3-hour averaged planetary index *Kp* (Figure 1h) shows an extended period of significant geomagnetic activity with a maximum *Kp* = 6^{+} at hour 39. The slow storm recovery lasted for

several days due to the continuing B_z fluctuations in the high speed flow behind the interaction region.

3. RAM-SCB Model Description

[9] The RAM-SCB model we use in this study couples two codes: (1) the ring current-atmosphere interactions model (RAM), which solves the bounce-averaged kinetic equation for the major ring current species [*Jordanova et al.*, 1997, 2006, 2010b], and (2) a 3-D Euler-potential-based plasma equilibrium code [*Zaharia et al.*, 2004, 2006, 2010; *Zaharia*, 2008]. In RAM-SCB, the plasma pressure produced by the ring current particles is used to calculate the resulting force-balanced magnetic field, which is then used to propagate the phase space distribution function. The 4-D kinetic RAM evaluates numerically the bounce-averaged distribution function for H^+, O^+, and He^+ ions and electrons in the magnetic equatorial plane as a function of radial distance from Earth (R_o from 2 to $6.5R_E$), all magnetic local times, kinetic energy from $\sim$100 eV to $\sim$400 keV, and equatorial pitch angle from $0°$ to $90°$. To set the initial conditions we use quiet time data from the instruments on the Polar satellite and run the model for more than 10 hours of quiet time before the storm commencement. The RAM numerical scheme and boundary conditions are described in detail by *Jordanova et al.* [1996]. In this study the nightside boundary conditions are determined from plasma sheet flux measurements from the MPA and SOPA instruments on the LANL geosynchronous spacecraft (Figure 1f). We preserve the local time dependence of the data and use the *Young et al.* [1982] study to correlate the ion composition with geomagnetic and solar activity. The dayside boundary conditions correspond to free particle outflow. Additional loss processes included in this study are charge exchange of ring current ions with geocoronal hydrogen, and ion and electron precipitation due to collisions with the dense atmosphere at low altitudes. Ring current electron losses inside the plasmasphere are calculated using electron lifetimes for pitch angle scattering by whistler mode hiss, lightning whistler, and VLF transmitters [*Abel and Thorne*, 1998; *Albert*, 1999], while losses due to whistler mode chorus scattering outside the plasmasphere are incorporated using electron lifetimes for diffusion that is not strong everywhere [after *Chen and Schulz*, 2001] (for further details, see *Jordanova et al.* [2008, 2010a]).

[10] The adiabatic transport and acceleration of both ring current ions and electrons are calculated under the conservation of the first and second adiabatic invariants, using time-dependent electric (**E**) and magnetic (**B**) field models updated at 5-min time intervals. To calculate the magnetic field we use a computational 3-D equilibrium approach in flux coordinates (Euler potentials) which is a direct extension [*Zaharia et al.*, 2004; *Zaharia*, 2008] of the isotropic pressure case [e.g., *Zaharia and Cheng*, 2003]. The numerical code solves the single-fluid plasma force-balance equation inside a computational domain bounded by an inner and outer magnetic flux surface obtained by field-line tracing using different empirical magnetic field models [*Zaharia et al.*, 2004, 2010]. For this study we used the *Tsyganenko and Sitnov* [2005] model parameterized by storm time data. In addition to the boundary specification, the 3-D equilibrium

code needs prescribed pressure profiles. We take perpendicular and parallel pressures in the equatorial plane as obtained from moments of the RAM distribution function and map the anisotropic RAM pressures along the 3-D magnetic field lines through energy and magnetic moment conservation. Only the pressure from ring current ions was used in our earlier magnetic field calculations as it is dominant; for this current simulation we have extended the model to include the electron pressure contribution as well. The electric field model in this study represents the gradient of the convection potential of W01 [*Weimer*, 2001] and a corotation potential. The W01 ionospheric potential is driven by interplanetary (IP) data (Figure 1) and the *AL* index and is mapped to the Solar Magnetic (SM) equatorial plane along SCB field lines.

[11] We calculate the linear growth rate of three dominant magnetospheric plasma waves driven by the free energy in the ring current distributions – EMIC, whistler mode chorus, and magnetosonic waves. The generation of EMIC waves in the equatorial plane is calculated as the ring current ion distributions evolve, using the hot plasma dispersion relation which is coupled and solved simultaneously with the kinetic equation. The density, parallel energy, and anisotropy of the ring current H^+, O^+, and He^+ ions used in the dispersion relation are calculated by taking moments of the distribution functions, while the cold plasma densities both inside and outside the plasmapause are obtained with the 2-D plasmasphere model of *Rasmussen et al.* [1993]. As in our previous studies the cold ion ratio is assumed to be 77% H^+, 20% He^+, and 3% O^+. The convective growth rate is calculated at every equatorial location as a function of frequency normalized to the proton cyclotron frequency (f_{cp}) and the maximum growth rate is selected. Recently we implemented algorithms in RAM to calculate the linear growth of whistler mode waves [*Jordanova et al.*, 2010a] and magnetosonic waves [*Chen et al.*, 2010b] – the latter are basically the low-frequency extension of whistler mode waves with wave normal angle close to $90°$. We use a dispersion relation [*Kennel and Petschek*, 1966; *Kennel*, 1966] which applies for arbitrary distribution functions and removes the need of fitting the particle distributions with bi-Maxwellian functions. We have now updated these calculations to use arbitrary magnetic field and compare RAM-SCB results with previous global simulation studies using dipolar magnetic field geometry [*Jordanova et al.*, 2010a; *Chen et al.*, 2010a, 2010b]. We note that wave-particle interactions are not included in this study so there is no plasma wave scattering feedback on the particle distributions.

4. Model Results and Discussion

4.1. Ring Current Dynamics

[12] We simulate ring current development during the 23–25 October 2002 HSS-driven storm using our coupled RAM-SCB model [*Jordanova et al.*, 2006, 2010b; *Zaharia et al.*, 2006, 2010], including for the first time the dynamics not only of ring current ions but also of ring current electrons. To demonstrate general characteristics of electron dynamics in various electric and magnetic field models, we show in Figure 2 the bounce-averaged rates of change for 100 keV electrons. The rates are obtained using VS [*Volland*, 1973; *Stern*, 1975] or W01 electric potential and
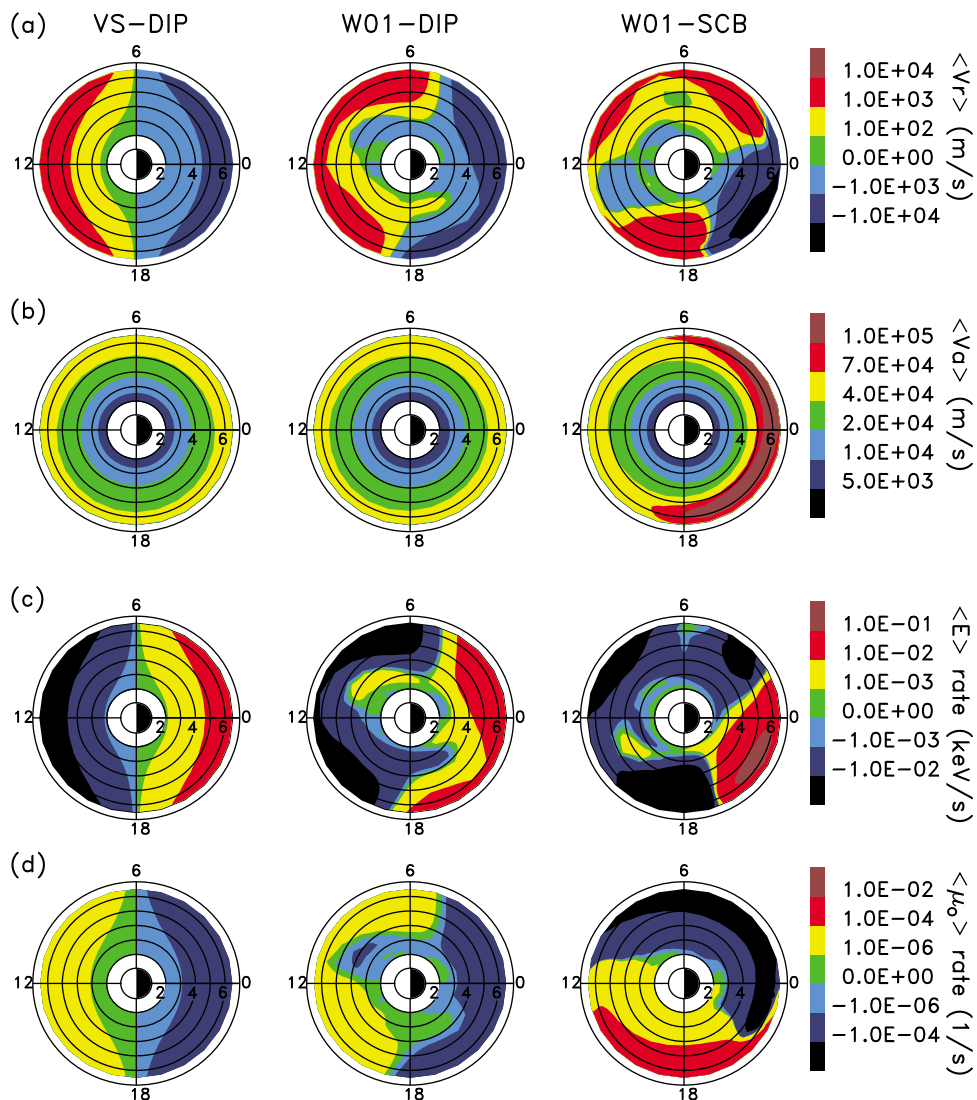
Figure 2. Parameters for 100 keV electrons with $\alpha_o = 45°$ at hour 32 using (left) Volland-Stern (VS) potential and dipolar B, (middle) Weimer (W01) potential and dipolar B, and (right) W01 potential and self-consistent B (SCB) model: (a) radial velocity component, (b) azimuthal velocity component, (c) rate of change of the kinetic energy E, and (d) rate of change of the cosine of particle's equatorial pitch angle μ_o.

either dipolar (DIP) or self-consistently calculated (SCB) magnetic field model. The Kp-dependent version [*Maynard and Chen*, 1975] of the VS model is used. From top to bottom are plotted the radial and azimuthal components of the $\mathbf{E} \times \mathbf{B}$ and magnetic gradient-curvature velocities, and the energy and μ_o (cosine of equatorial pitch angle) rates of change for particles with 45° equatorial pitch angle, during the storm main phase at hour 32. For 100 keV electrons the radial component (Figure 2a) is dominated by the $\mathbf{E} \times \mathbf{B}$ drift, while the azimuthal component (Figure 2b) is dominated by the magnetic gradient-curvature drift. The energy (Figure 2c) and μ_o (Figure 2d) rates of change indicate, respectively, the acceleration of the particles and the change of their pitch angle along the drift paths. All four rates of change are symmetric in the VS-DIP case due to the symmetry of the used electric and magnetic fields; the asymmetry in the W01-DIP case reflects the small-scale

variations of the W01 electric field, while the asymmetry in the W01-SCB case reflects variations in the magnetic field as well. All electron rates increase significantly at large radial distances ($R_o > 4R_E$) in the midnight to dusk MLT sector when the self-consistent magnetic field is used, due to the decreased intensity of $\mathbf{B}$ in comparison with a dipolar field. This is because, similarly to the ion rates [see *Jordanova et al.*, 2010b, equations 2 and 5], when the equatorial electric field is kept the same (as we do in the W01 simulations) the electron rates are inversely proportional to the magnetic field intensity. The electrons, however, drift eastward (Figure 2b) in opposite direction to the ions and their pitch angles increase as the electrons drift from midnight through dawn to noon and decrease when they drift from noon through dusk and back to midnight (Figure 2d). Since the rates are pitch angle dependent, particles with different pitch angles starting on the same
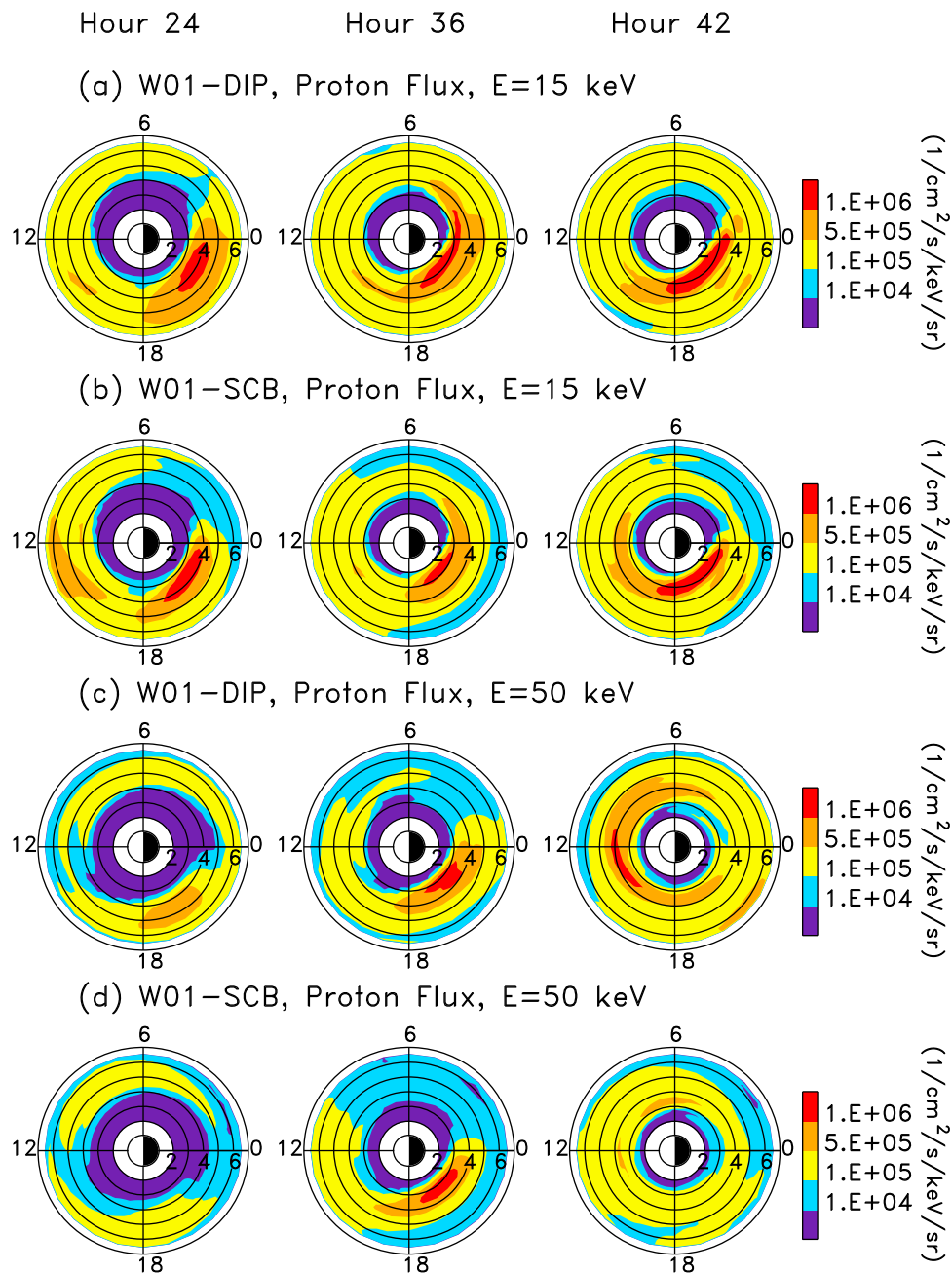
Figure 3. Ion fluxes (1/cm^2/s/keV/sr) for (a–b) 15 keV and (c–d) 50 keV energy at hours 24, 36, and 42, and 60° equatorial pitch angle as a function of radial distance in the equatorial plane and MLT using Weimer (W01) electric field, and either dipolar (DIP) or self-consistent (SCB) magnetic field.

field line will undergo drift-shell splitting [e.g., *Roederer*, 1970] and will populate different shells as they drift around the Earth. The effect is greater for particles mirroring close to the equator (near 90° pitch angle); after being injected at midnight these particles will drift outward to larger L shells on the dayside and may get lost through the magnetopause (process known as magnetopause shadowing [e.g., *Sibeck et al.*, 1987]). In summary, in a nondipolar field both ions and electrons experience drift-shell splitting, and drift faster through the nightside magnetosphere undergoing larger acceleration. This will cause significant differences in the energy and pitch angle

distributions of the ring current particles compared to drifts in a dipolar magnetic field.

[13] We start the simulation of the HSS-driven storm interval at quiet time (hour 10), about 14 hours before the storm commencement, and let it evolve into storm time. Calculated equatorial proton and electron fluxes are shown at three representative times during this period, hour 24 (quiet time), hour 36 (main phase), and hour 42 (near *Dst* minimum), in Figures 3 and 4, respectively. We compare results from simulations using W01 [*Weimer*, 2001] electric potential and either dipolar or self-consistent magnetic field model. The ion and electron fluxes intensify
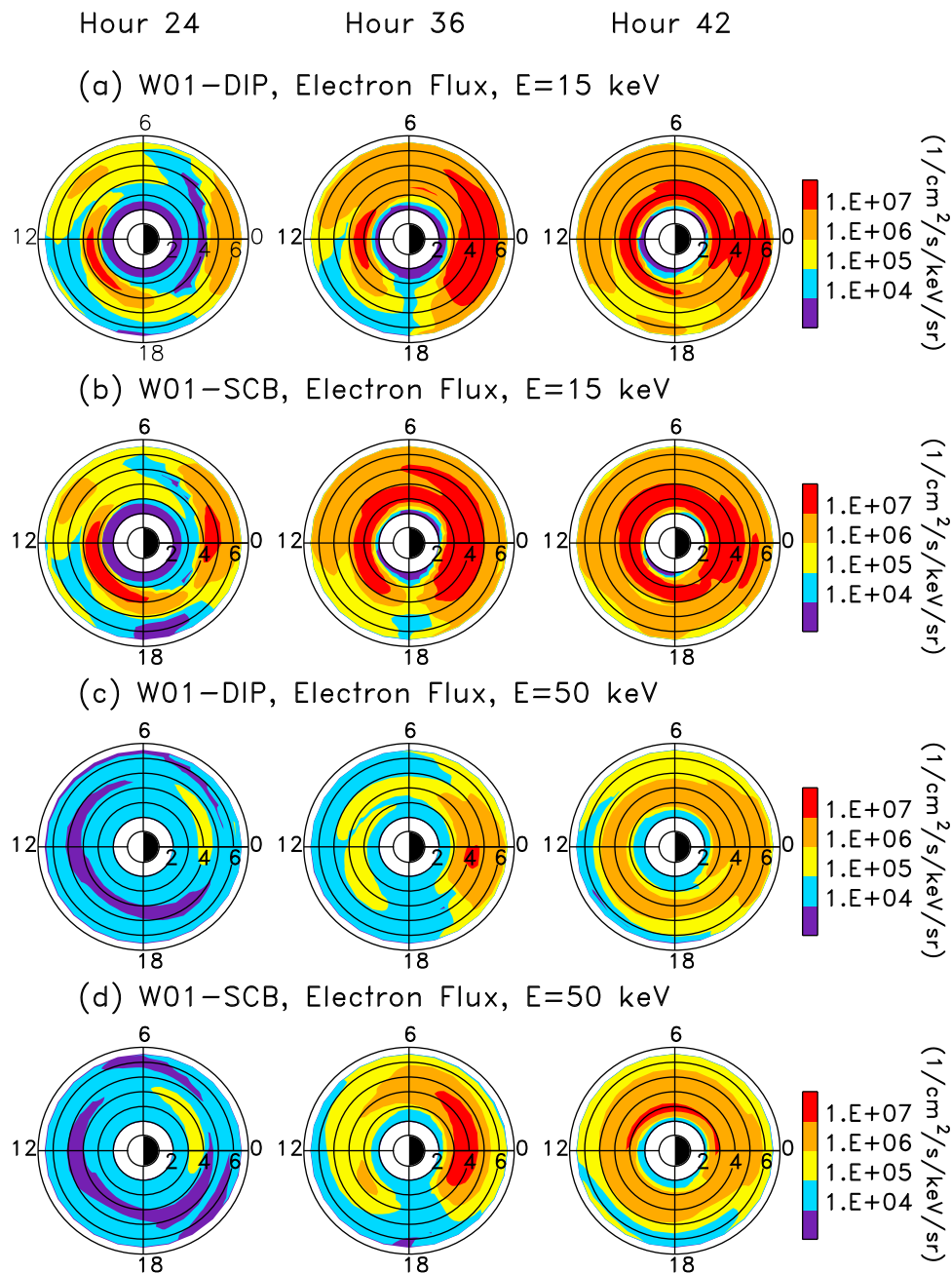
Figure 4. Electron fluxes (1/cm^2/s/keV/sr) for (a–b) 15 keV and (c–d) 50 keV energy at hours 24, 36, and 42, and 60° equatorial pitch angle as a function of radial distance in the equatorial plane and MLT using Weimer (W01) electricfield, and either dipolar (DIP) or self-consistent (SCB) magnetic field.

with storm development as the particles are injected from the plasma sheet, accelerated, and trapped. The ion fluxes peak in the premidnight MLT sector, while the electron fluxes peak near midnight. The lower energy (15 keV) particles penetrate deeper (reaching $\approx 2R_E$ at hour 42) and their fluxes are larger than these of the higher energy (50 keV) particles. As shown in previous studies [e.g., *Jordanova et al.*, 2010b] the ion fluxes (Figure 3) decrease on the nightside when a nondipolar magnetic field is used; this is clearly seen especially at larger distances (>5R_E). A different behavior is observed for the ring current electron fluxes (Figure 4); although they do decrease at larger (>5R_E) distances on the

nightside, the electron fluxes actually increase close to Earth when a self-consistent magnetic field is used. This is caused by the increased drift velocities in the dusk to midnight MLT sector (Figure 2) combined with the eastward electron drift leading to deeper penetration and trapping of the electrons in asymmetric electric and magnetic fields. The electron fluxes are larger and become symmetric at hour 42 for both energies at $R_o < 4R_E$ in the SCB simulation. These electron dynamics are in agreement with the recent study of *Li et al.* [2010] which presented evidence from THEMIS data of plasma sheet electron entry into the plasmasphere during disturbed geomagnetic conditions.
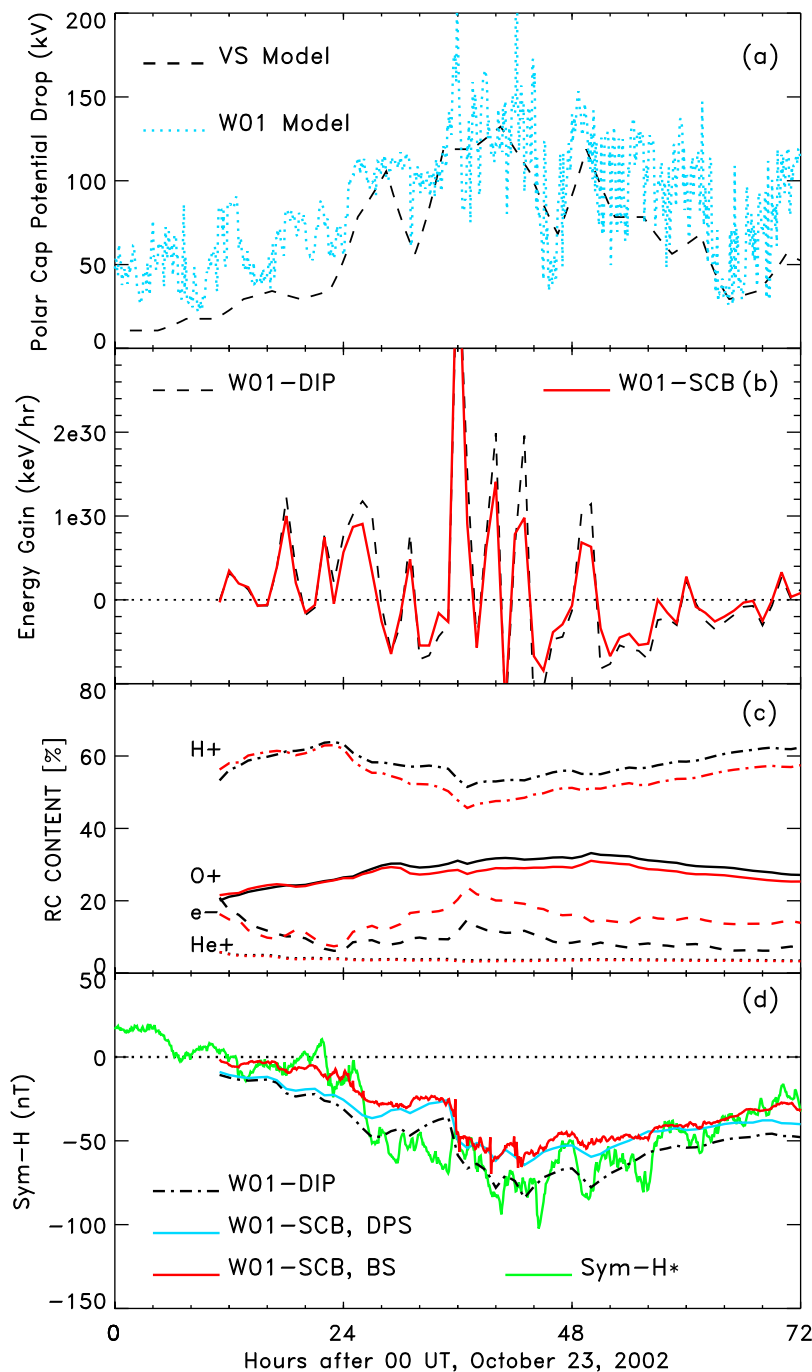
Figure 5. (a) Cross polar cap potential obtained with the IP-dependent model of Weimer (W01) (dotted line) and the *Kp*-dependent Volland-Stern model (dashed line). (b) Ring current injection rate (keV/hr) calculated with the W01-DIP (dashed), or W01-SCB (solid) model. (c) Contribution to total ring current energy from various species during W01-DIP (black) or W01-SCB (red) simulations. (d) Computed *Dst* index using different model formulations compared with magnetopause current-corrected SYM-H (solid green) during 23–25 October 2002.

[14] The global ring current evolution in response to the HSS driving is shown in Figure 5. The top panel displays the cross polar cap potential (CPCP) obtained with VS model using 20° magnetic colatitude of the polar cap boundary [*Stern*, 1975] and with W01 model as the difference between the maximum and minimum potential values. The VS model is interpolated linearly to make a smooth transition between the different *Kp* levels. It shows three intensifications above ~100 kV coincident with *Kp* increases (Figure 1h) at hours ~28.5, 40.5, and 49.5. The W01 model depends on IP conditions and exhibits many small-scale fluctuations, rising quickly above 100 kV during the southward IMF *Bz* turning at hour ~25, intensifying during the stream-stream interaction at hour 36 and staying elevated at an average level of

~135 kV until hour ~44, and rising again to ~150 kV during the southward IMF B_z turning at hour ~48; all these CPCP increases correspond to the IEF intensifications shown in Figure 1e. The interplay between the magnitudes of magnetospheric convection and plasma sheet density (Figure 1f) determines the ring current evolution as clearly seen in the ring current injection rates plotted in Figure 5b whose peaks (drops) correspond to increases (decreases) of these values. Comparisons of simulations using W01 potential and either dipolar or self-consistent **B** field indicate that the energy gain (Figure 5b) is smaller in the latter case due to the reduced proton fluxes (Figure 3). The contribution to the total ring current energy from various species is shown in Figure 5c. The major contribution is from H^+, which is the dominant species, and it varies between 60% at the beginning of the storm at hour 24 and ~50% during the HSS interface. The ring current O^+ content gradually increases and reaches a maximum of ~30% near minimum *Dst*, while He^+ content remains at ~5% throughout the interval. On the other hand, the electron content is quite variable, being about 10% during quiet time and about 20% during disturbed time. Note that it is significantly larger in the W01-SCB case than in the W01-DIP case due to more efficient electron injection and trapping in nondipolar magnetic fields as indicated from the flux enhancement at small radial distances in Figure 4. Finally, the total ring current contribution to the *Dst* index is shown in Figure 5d. We compare results computed with the Dessler-Parker-Sckopke (DPS) relation [*Dessler and Parker*, 1959; *Sckopke*, 1966], or a Biot-Savart (BS) integration of the currents in the whole domain, with the SYM-H index (the high-resolution analog of *Dst*). The computation using DPS relation is strictly valid for a dipolar magnetic field and is performed with 1 hour time resolution; it has smoother variations than the one using BS integration performed at 5-min time cadence. The observed SYM-H is corrected for magnetopause current contribution after the study of *Burton et al.* [1975]. Overall the global evolution of the ring current reproduces very well the temporal variations of SYM-H. As discussed above larger ring current injection and, correspondingly, SYM-H depression, is obtained using a dipolar **B** field (dash-dotted line). In agreement with previous studies [e.g., *Chen et al.*, 2006; *Jordanova et al.*, 2010b], the ring current contribution to *Dst* is about 25% smaller in the self-consistent **B** (solid line) simulation; it underestimates minimum |SYM-H| but reproduces very well the storm recovery phase. Note that contributions from tail currents outside geosynchronous orbit, estimated to be ~25% by *Turner et al.* [2000] are not included in this study. The Biot-Savart calculation reproduces better SYM-H variations than the DPS relation during the initial storm period when the current intensity (proportional to the pressure gradient) is small while the plasma pressure itself is non-negligible; the difference between the two formulations is small once a significant current builds up after hour ~28.

4.2. Plasma Wave Dynamics

[15] We calculated the linear growth rate of three dominant magnetospheric plasma waves excited by the aniso-tropic electron and ion ring current populations as the HSS-driven storm develops. The growth rate of whistler mode chorus was calculated in the equatorial plane as a function of frequency normalized to the equatorial electron cyclotron frequency (f_{ce}) between 0.1 and 0.7 f_{ce} for the case of waves propagating parallel to the magnetic field (wave normal angle of 0°). Representative growth rate of chorus with frequency 0.45 f_{ce} obtained at hours 24, 28, and 32, with W01-DIP or W01-SCB model simulations is plotted in Figures 6a and 6b, respectively. The growth rate increases in the W01-SCB case at first in the postmidnight MLT sector (hour 24) as the plasma sheet electrons penetrate inside of geosynchronous orbit on the nightside, and then the intense chorus growth moves to the dayside as the electrons are transported eastward (hours 28 and 32). The growth rate is more than an order of magnitude larger in the self-consistent **B** simulations (Figure 6b) than in the dipolar ones (Figure 6a). This is due to the bigger anisotropy ($A > 1$) that develops at larger radial distances prenoon in a nondipolar magnetic field (Figure 6d) due to drift-shell splitting, since higher pitch angle particles move outward while drifting from midnight to noon. As particles with larger pitch angles may intercept the magnetopause, electrons with near 90° pitch angles will be depleted from the outer postnoon to midnight magnetosphere and the anisotropy becomes negative in this MLT region with storm development (Figure 6d, middle). In agreement, pancake (peak at 90°) pitch angle distributions dominate the dayside magnetosphere while butterfly (minimum at 90°) electron pitch angle distributions are often observed at large *L* shells in the afternoon to midnight magnetosphere [e.g., *Sibeck et al.*, 1987]. The dayside anisotropy is sufficient to excite both lower-band and upper-band chorus with normalized frequency between ~0.3 and 0.7 f_{ce}. Note that this study does not consider wave-induced diffusion, the pitch angle anisotropy and subsequent wave growth may be reduced when this feedback is taken into account. The electron anisotropy is reduced on the nightside as the storm develops and there is no significant nightside chorus excitation. We have used isotropic flux boundary conditions in these simulations; larger wave growth is predicted in the premidnight to dawn MLT sector even in the dipolar case when the electron fluxes at the nightside boundary are anisotropic [*Jordanova et al.*, 2010a]. The plasmaspheric density, the ratio of plasma frequency (f_{pe}) to cyclotron frequency (f_{ce}), and parallel energy of resonant particles are shown in Figure 7 for the self-consistent **B** field simulation. In agreement with previous chorus observations [*Meredith et al.*, 2003; *Li et al.*, 2010] the wave growth maximizes outside the plasmasphere where the f_{pe}/f_{ce} ratio ranges from ~4 to 6. The resonant electrons have parallel energy from ~1 to 6 keV. For example, the large growth rate obtained at $R_o > 4R_E$ in the postmidnight sector at hour 24 is caused by injected electrons with resonant energy of ~4 keV and anisotropy $A \approx 2$. The strong linear growth predicted in the self-consistent **B** simulations should be sufficient to excite further nonlinear growth to a saturation level and this will be investigated in future studies.

[16] Anisotropic ring current ion populations that develop after the storm time particle injection from the plasma sheet are unstable to the excitation of EMIC and magnetosonic waves. To demonstrate the evolution of ion-generated plasma waves during the HSS-driven interval, we first display RAM-SCB simulations of EMIC waves at selected hours (28, 36, and 48) in Figure 8. In agreement with previous studies, enhanced EMIC wave growth occurs in the equatorial plane within regions of spatial overlap of energetic
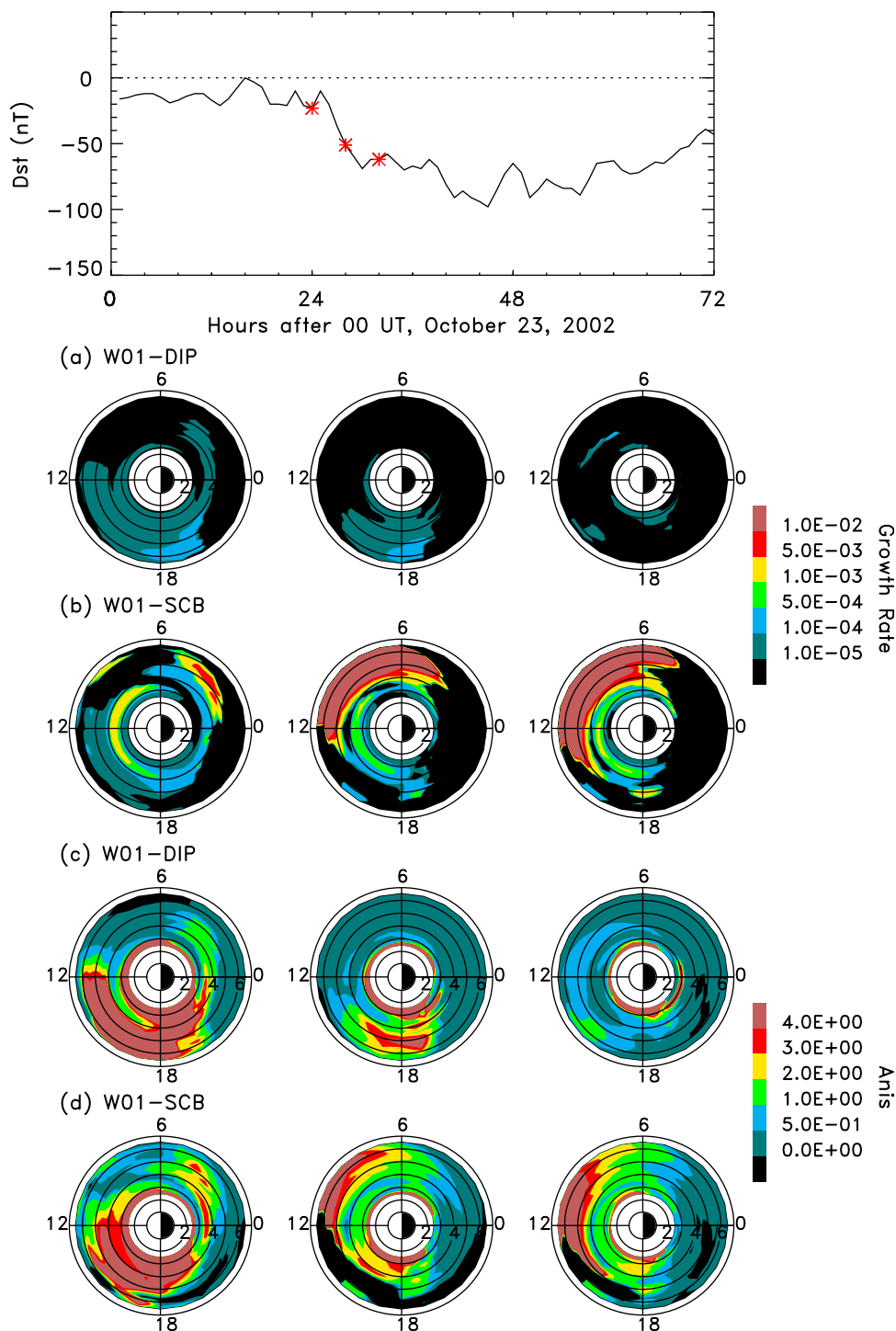
Figure 6. Normalized growth rate of whistler mode chorus with frequency $0.45 f_{ce}$ calculated with RAM-SCB using W01 electric field and (a) dipolar magnetic field or (b) self-consistently calculated magnetic field in the equatorial plane at selected hours after 00 UT 23 October 2002 indicated with stars in the *Dst* plot. The corresponding effective anisotropy is plotted in Figures 6c and 6d, respectively.

ring current ions and high-density plasmaspheric populations on the duskside [*Jordanova et al.*, 1997, 2001; *Thorne and Horne*, 1997; *Chen et al.*, 2010a]. During this HSS interval intense He$^+$ band (between O$^+$ and He$^+$ gyrofrequencies) EMIC waves are predicted in a limited spatial range at $R_o > 5R_E$ in the postnoon MLT sector and along the duskside

plasmapause only when a self-consistent magnetic field model is used (Figure 8b, hours 28 and 36). The wave frequencies corresponding to the maximum wave growth at $R_o > 5R_E$ are between ~ 0.13 and $0.19 f_{cp}$ while these at smaller radial distances correspond to $\sim 0.22 f_{cp}$. By analogy to the electron case, the ring current ion anisotropy increases
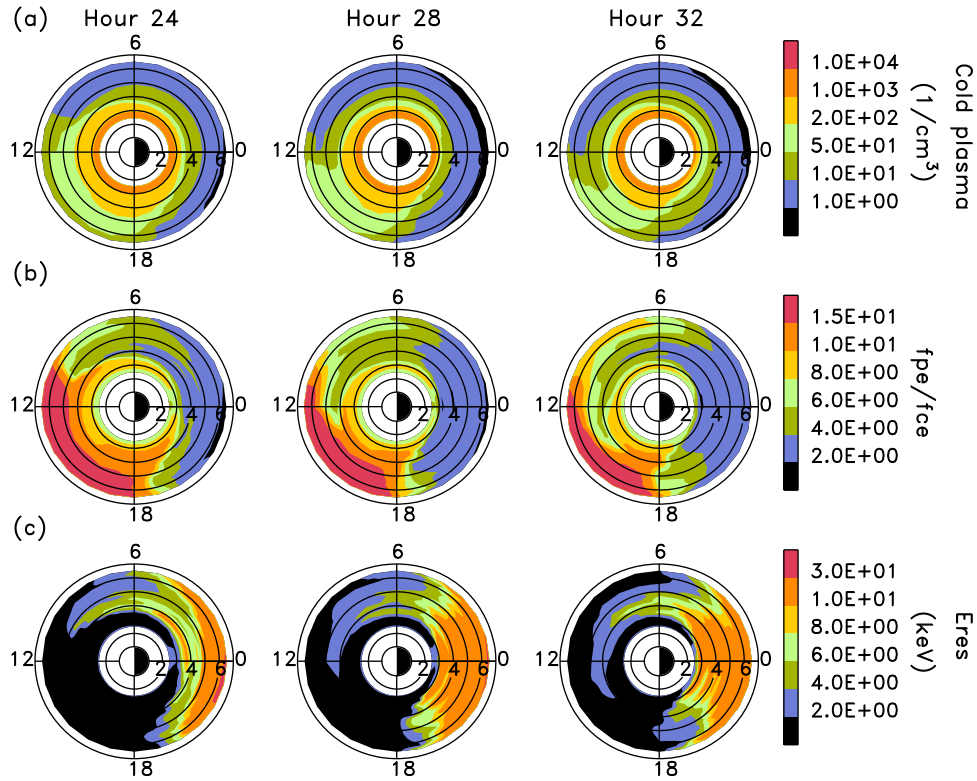
Figure 7. (a) The plasmaspheric electron density, (b) the ratio of plasma frequency to cyclotron frequency, and (c) parallel energy of electrons resonating with 0.45 f_{ce} whistler mode chorus from the W01-SCB simulation as a function of radial distance in the equatorial plane and MLT at selected hours after 00 UT 23 October 2002.

at large radial distances in the postnoon sector (Figure 8d) as the ions drift westward from the nightside in nondipolar magnetic fields [*Jordanova et al.*, 2010b]. The anisotropy decreases in the prenoon sector and on the nightside due to the drift-shell splitting and magnetopause shadowing processes discussed above. The values of the electron and ion anisotropies differ since these particles undergo different injection (as indicated from the geosynchronous fluxes) and loss processes, and follow different transport paths. The ion anisotropy is large close to Earth in both dipolar and self-consistent **B** simulations due to charge exchange losses but this does not lead to any significant EMIC waves excitation (Figures 8a and 8b) since the ion energy necessary for resonance with these waves is too high [*Jordanova et al.*, 1997]. The wave growth rates decrease as the ring current decays during the recovery phase (hour 48). The predicted intense EMIC waves (with convective growth rate larger than $\sim 10^{-8}$ cm^{-1}) will cause significant scattering loss of ring current ions and radiation belt electrons [*Jordanova et al.*, 2008; *Chen et al.*, 2010a].

[17] Figure 9 shows the excitation of magnetosonic waves at selected hours (28, 32, 44) during the HSS-driven storm, comparing results from simulations using a dipolar or a self-consistently calculated magnetic field. Following the theoretical analysis of *Chen et al.* [2010b], we calculate the convective growth rate (along the direction of the wave group velocity) of highly oblique magnetosonic waves with wave normal angle $\sim 89.5°$. This wave normal angle is chosen because (1) electron Landau damping is strong for

small wave normal angles and restricts the magnetosonic wave generation to angles greater than 85°, and (2) the growth rate is not sensitive to the choice of wave normal angle for large (>89°) angles [*Horne et al.*, 2000; *Chen et al.*, 2010b]. The maximum convective growth rate magnitude of $\sim 10^{-7}$ cm^{-1} is similar in the dipolar (Figure 9a) and self-consistent **B** case (Figure 9b), but it has a larger spatial extent in the SCB simulation. The growth rate increases in the prenoon MLT sector at first (hour 28) outside the plasmasphere at $R_o > 4R_E$ and it expands later as the storm develops (hour 32) into the afternoon and dawn sectors at $R_o > 3.5R_E$. Near minimum *Dst* (hour 44) there is substantial growth at $R_o \approx 4R_E$ premidnight and inside the plasmasphere between MLT ≈ 6 and MLT ≈ 12. The free energy for exciting magnetosonic waves is provided by the proton rings with positive slopes ($\partial f / \partial v_\perp > 0$) in the phase space density; negative slopes contribute to wave damping. In addition, linear theory predicts that the wave growth is small if the speed of the peak phase space density of the ring (V_R) is not within a factor of 2 of the Alfvén speed (V_A) [e.g., *Horne et al.*, 2000]. These conditions determine where magnetosonic waves are preferentially excited in the equatorial magnetosphere. Ion ring-type distributions develop as a result of energy dependent drift and loss of injected ions. A minimum (called stagnation dip) [*Lennartsson et al.*, 1979] forms in the ion velocity distributions at ~ 10 keV because of the large losses undergone by the slowly drifting ring current ions at these energies. The stagnation dips occur predominantly on the dayside and are seen both in observations and
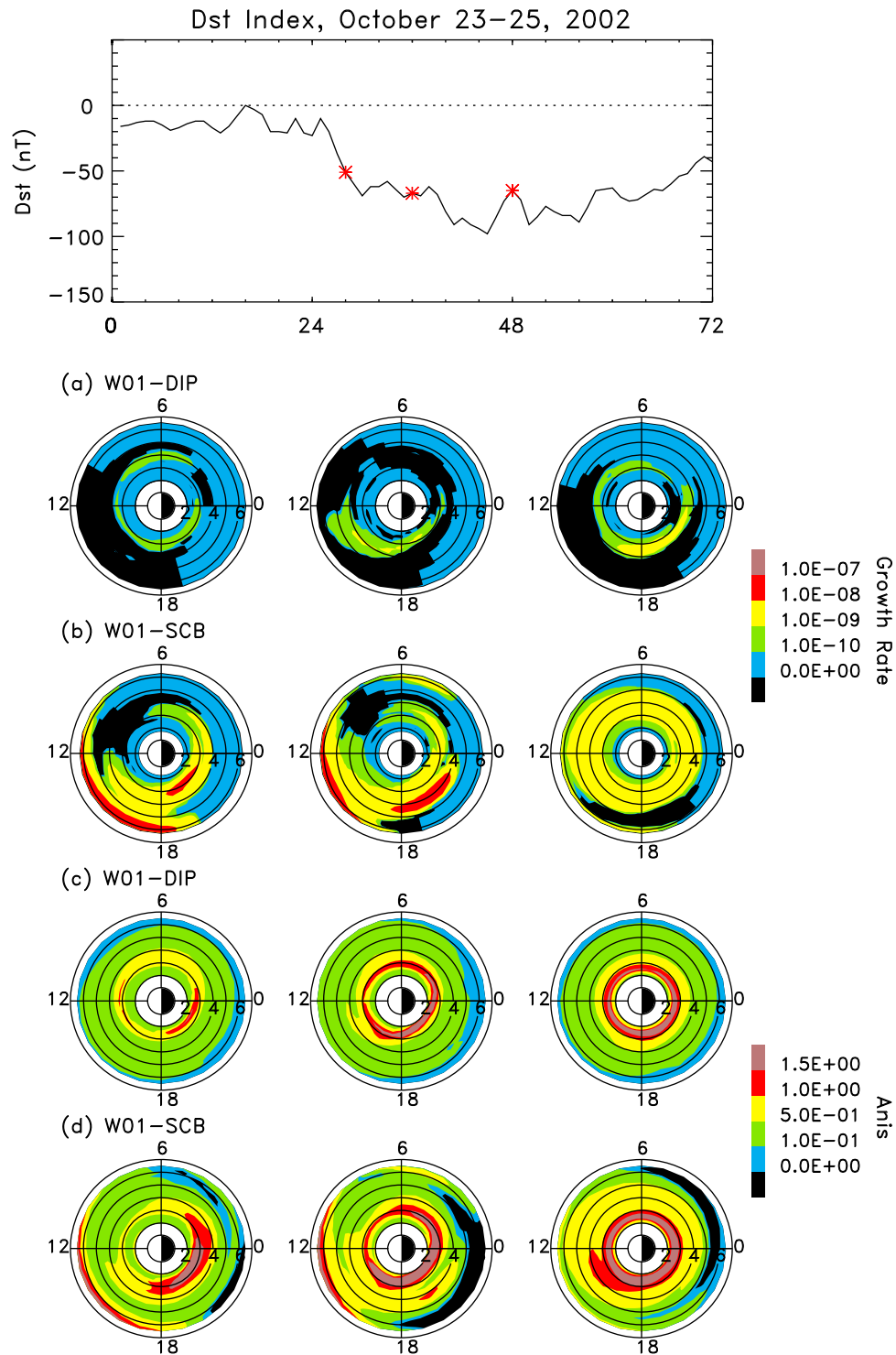
Figure 8. Convective growth rate (1/cm) of He$^+$ band EMIC waves calculated with RAM-SCB using W01 electric field and (a) dipolar or (b) self-consistently calculated magnetic field in the equatorial plane at selected hours after 00 UT 23 October 2002 indicated with stars in the *Dst* plot. The corresponding proton anisotropy is plotted in Figures 8c and 8d, respectively.

simulations [e.g., *Kistler et al.*, 1989; *Jordanova et al.*, 1999]. *Chen et al.* [2010b] demonstrated that the formation of such ring-type distributions in a dipolar magnetic field leads to magnetosonic wave excitation over a broad spatial range on the dayside from dawn to dusk. In a nondipolar magnetic field the charge exchange losses are stronger on the dayside [*Jordanova et al.*, 2010b], leading to larger gradients in the phase space density and therefore to a larger wave growth (Figure 9b). The intense growth in the premidnight sector at hour 44 is caused by a dispersed injection observed
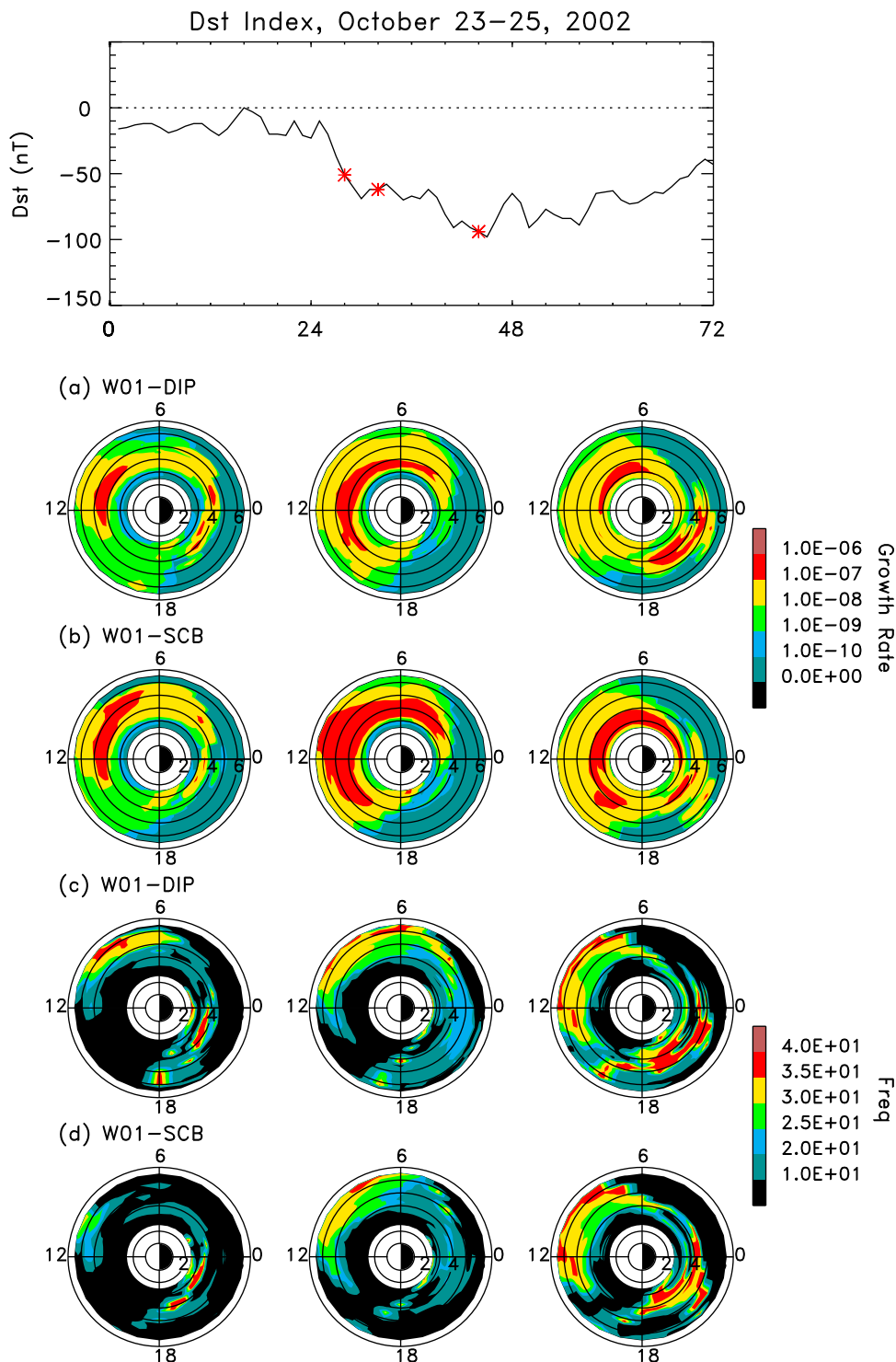
Figure 9. Convective growth rate (1/cm) of magnetosonic waves calculated with RAM-SCB using W01 electric field and (a) dipolar or (b) self-consistently calculated magnetic field in the equatorial plane at selected hours after 00 UT 23 October 2002 indicated with stars in the *Dst* plot. The corresponding normalized wave frequency is plotted in Figures 9c and 9d, respectively.

with the geosynchronous LANL instruments (higher energy ions arriving earlier at the spacecraft, consistent with previous studies [e.g., *Chen et al.*, 2011]) and propagating earthward. The frequency of the excited waves depends on the ratio V_R/V_A, where the waves grow at higher frequencies for smaller ratios (in the lower density region outside the plasmasphere). The corresponding normalized wave frequency is thus between ~10 and 35 f_{cp} and it increases with R_o as the cold plasma density decreases (Figures 9c and 9d). The spatial extent of the unstable distributions compares

reasonably well with the statistical survey of *Meredith et al.* [2008], who found that magnetosonic waves are observed over a broad MLT range outside the plasmapause and in the afternoon to premidnight sector inside the plasmapause (note that CRRES had a limited coverage on the dayside).

5. Summary and Conclusions

[18] We studied the response of the inner magnetosphere to the HSS passage at Earth during 23–25 October 2002. We used our RAM-SCB model developed further to include the dynamics of ring current electrons and a 2-D (L, MLT) time-dependent plasmasphere model. The RAM-SCB model includes two codes: the ring current-atmosphere interactions model that solves the bounce-averaged kinetic equation for H^+, O^+, He^+ ions and electrons in the equatorial plane, and the 3-D Euler-potential-based plasma equilibrium code that calculates self-consistently the magnetic field in force balance with the anisotropic ring current distributions. Comparisons of RAM-SCB model results with spacecraft observations are presented in the validation study by *Yu et al.* [2012]. To demonstrate how the magnetic field configuration affects the ring current evolution we compared results from simulations using either dipolar or self-consistently calculated magnetic field. The W01 model mapped to the equatorial plane along SCB field lines was used to provide the time-dependent convection electric field as a function of interplanetary parameters. We investigated the dynamics of both ring current ions and electrons since most of the interest in the community in recent years has focused only on the dynamics of ring current ions as the main carriers of the inner magnetosphere plasma pressure. We investigated also three plasma instabilities driven by the free energy in the ring current distributions in the equatorial plane and leading to the generation of magnetosonic, EMIC, and whistler mode chorus waves. These waves play an essential role for the acceleration and loss of ring current and radiation belt particles.

[19] There are several important findings from this study.

[20] 1. The ion and electron fluxes intensified in both the dipolar and self-consistent simulations as the storm developed. The electron dynamics in a nondipolar **B** field at large radial distances from Earth were similar to the ion dynamics [*Jordanova et al.*, 2010b], leading to decreased fluxes on the nightside and confinement of the ring current close to Earth. However, the ion and electron dynamics were quite different at smaller radial distances, where the electron fluxes increased while the ion fluxes decreased compared to the dipolar simulations. The ring current intensification in the premidnight region with storm evolution caused strong depression of the self-consistently calculated magnetic field. This led to increased velocities in the premidnight sector (as they are inversely proportional to the magnetic field intensity) and to more efficient injection and trapping of plasma sheet electrons as they drifted in asymmetric electric and magnetic fields.

[21] 2. The major ring current species during this HSS interval was H^+; O^+ provided about 30% of the total ring current energy, while He^+ provided about 5%. Note that since the ring current electron penetration to low R_o was significantly enhanced in the self-consistent simulations, the electron contribution increased from ∼10% to 20% as the storm developed.

[22] 3. An increased inflow of plasma sheet ions and electrons occurred during the storm main phase; these particles were transported earthward and energized by an enhanced convection electric field, and drifted azimuthally around the Earth (in opposite directions for electrons and ions) to form an intensified ring current. In agreement with previous studies the ring current intensity as well as its contribution to *Dst* were smaller in the nondipolar simulation than in the dipolar one. The *Dst* calculation results using a Biot-Savart integration were similar to the ones using the DPS relation except during quiet time when the Biot-Savart calculation reproduced better SYM-H variations. The SCB simulation underestimated minimum |SYM-H| index with ∼25% but reproduced well the recovery phase. Better agreement is expected when contributions from tail currents outside geosynchronous orbit are included.

[23] 4. The anisotropy of both ring current ions and electrons increased significantly at large distances from Earth on the dayside as particles drifted in nondipolar **B** field. As the storm developed, sufficient free energy was available in the ring current distributions to excite whistler mode chorus, magnetosonic, and EMIC waves in the equatorial magnetosphere.

[24] 5. Therefore, the growth rate of plasma waves increased significantly in the self-consistent magnetic field simulations. The waves were generated after the storm time injection of plasma sheet particles inside of geosynchronous orbit and exhibited quite different local time distribution. While EMIC waves were usually excited at large ($>5R_E$) radial distances on the duskside or along the plasmapause, chorus waves were predominantly excited outside the plasmasphere on the dawnside, and magnetosonic waves were excited at different locations both inside and outside the plasmasphere throughout the storm interval.

[25] It should be noted that in the simulations of plasma wave excitation presented in this study we have not specifically considered wave-particle pitch angle scattering and energy diffusion. We expect the ring current populations to become more isotropic and the wave growth to be reduced once a plasma wave scattering feedback is taken into account. As discussed in the introduction, both ring current and radiation belt particles will be subject to energy and pitch angle diffusion by these waves. For example, as the electrons drift around the Earth they may be scattered by chorus on the nightside, magnetosonic waves in the prenoon sector and EMIC waves in the postnoon sector. The effects from these plasma wave dynamics on ring current and radiation belt evolution will be addressed in future extensions of this work.

References

Abel, B., and R. M. Thorne (1998), Electron scattering loss in Earth's inner magnetosphere: 1. Dominant physical processes, *J. Geophys. Res.*, *103*, 2385–2396.

Albert, J. M. (1999), Analysis of quasi-linear diffusion coefficients, *J. Geophys. Res.*, *104*, 2429–2441.

Borovsky, J., M. Thomsen, and D. McComas (1997), The superdense plasma sheet: Plasmaspheric origin, solar wind origin, or ionospheric origin?, *J. Geophys. Res.*, *102*, 22,089–22,097.

Bortnik, J., R. M. Thorne, and N. P. Meredith (2008), The unexpected origin of plasmaspheric hiss from discrete chorus emissions, *Nature*, *452*, 62–66, doi:10.1038/nature06741.

Burton, R., R. McPherron, and C. Russell (1975), An empirical relationship between interplanetary conditions and *Dst*, *J. Geophys. Res.*, *80*, 4204–4214.

Chen, L., R. M. Thorne, V. K. Jordanova, C.-P. Wang, M. Gkioulidou, L. Lyons, and R. B. Horne (2010a), Global simulation of EMIC wave excitation during the 21 April 2001 storm from coupled RCM-RAM-HOTRAY modeling, *J. Geophys. Res.*, *115*, A07209, doi:10.1029/2009JA015075.

Chen, L., R. M. Thorne, V. K. Jordanova, and R. B. Horne (2010b), Global simulation of magnetosonic wave instability in the storm time magnetosphere, *J. Geophys. Res.*, *115*, A11222, doi:10.1029/2010JA015707.

Chen, L., R. M. Thorne, V. K. Jordanova, M. F. Thomsen, and R. B. Horne (2011), Magnetosonic wave instability analysis for proton ring distributions observed by the LANL magnetospheric plasma analyzer, *J. Geophys. Res.*, *116*, A03223, doi:10.1029/2010JA016068.

Chen, M. W., and M. Schulz (2001), Simulations of storm time diffuse aurora with plasmasheet electrons in strong pitch angle diffusion, *J. Geophys. Res.*, *106*, 1873–1886.

Chen, M. W., S. Liu, M. Schulz, J. L. Roeder, and L. R. Lyons (2006), Magnetically self-consistent ring current simulations during the 19 October 1998 storm, *J. Geophys. Res.*, *111*, A11S15, doi:10.1029/2006JA011620.

Daglis, I. A., R. M. Thorne, W. Baumjohann, and S. Orsini (1999), The terrestrial ring current: Origin, formation, and decay, *Rev. Geophys.*, *37*, 407–438.

Dessler, A. J., and E. N. Parker (1959), Hydromagnetic theory of geomagnetic storms, *J. Geophys. Res.*, *64*, 2239–2252.

Elkington, S. R., et al. (2003), Resonant acceleration and diffusion of outer zone electrons in an asymmetric geomagnetic field, *J. Geophys. Res.*, *108* (A3), 1116, doi:10.1029/2001JA009202.

Erlandson, R., and A. J. Ukhorskiy (2001), Observations of electromagnetic ion cyclotron waves during geomagnetic storms: Wave occurrence and pitch angle scattering, *J. Geophys. Res.*, *106*, 3883–3895.

Frank, L. A. (1967), On the extraterrestrial ring current during geomagnetic storms, *J. Geophys. Res.*, *72*, 3753–3767.

Fraser, B. J., H. J. Singer, W. J. Hughes, J. R. Wygant, R. R. Anderson, and Y. D. Hu (1996), CRRES Poynting vector observations of electromagnetic ion cyclotron waves near the plasmapause, *J. Geophys. Res.*, *101*, 15331–15343, doi:10.1029/95JA03480.

Hairston, M. R., T. W. Hill, and R. A. Heelis (2003), Observed saturation of the ionospheric polar cap potential during the 31 March 2001 storm, *Geophys. Res. Lett.*, *30*(6), 1325, doi:10.1029/2002GL015894.

Horne, R. B., and R. M. Thorne (1993), On the preferred source location for the convective amplification of ion cyclotron waves, *J. Geophys. Res.*, *98*, 9233–9247.

Horne, R. B., and R. M. Thorne (1997), Wave heating of He$^+$ by electromagnetic ion cyclotron waves in the magnetosphere: Heating near the H$^+$-He$^+$ bi-ion resonance frequency, *J. Geophys. Res.*, *102*, 11,457–11,471.

Horne, R. B., and R. M. Thorne (1998), Potential waves for relativistic electron scattering and stochastic acceleration during magnetic storms, *Geophys. Res. Lett.*, *25*, 3011–3014.

Horne, R. B., G. V. Wheeler, and H. St. C. K. Alleyne (2000), Proton and electron heating by radially propagating fast magnetosonic waves, *J. Geophys. Res.*, *105*, 27,597–27,610.

Horne, R. B., R. M. Thorne, S. A. Glauert, N. P. Meredith, D. Pokhotelov, and O. Santolík (2007), Electron acceleration in the Van Allen radiation belts by fast magnetosonic waves, *Geophys. Res. Lett.*, *34*, L17107, doi:10.1029/2007GL030267.

Jordanova, V. K., and Y. Miyoshi (2005), Relativistic model of ring current and radiation belt ions and electrons: Initial results, *Geophys. Res. Lett.*, *32*, L14104, doi:10.1029/2005GL023020.

Jordanova, V. K., L. M. Kistler, J. U. Kozyra, G. V. Khazanov, and A. F. Nagy (1996), Collisional losses of ring current ions, *J. Geophys. Res.*, *101*, 111–126.

Jordanova, V. K., J. U. Kozyra, A. F. Nagy, and G. V. Khazanov (1997), Kinetic model of the ring current-atmosphere interactions, *J. Geophys. Res.*, *102*, 14,279–14,292, doi:10.1029/96JA03699.

Jordanova, V. K., C. J. Farrugia, J. M. Quinn, R. B. Torbert, J. E. Borovsky, R. B. Sheldon, and W. K. Peterson (1999), Simulation of off-equatorial ring current ion spectra measured by POLAR for a moderate storm at solar minimum, *J. Geophys. Res.*, *104*, 429–436.

Jordanova, V. K., C. J. Farrugia, R. M. Thorne, G. V. Khazanov, G. D. Reeves, and M. F. Thomsen (2001), Modeling ring current proton precipitation by electromagnetic ion cyclotron waves during the May 14–16, 1997, storm, *J. Geophys. Res.*, *106*, 7–22.

Jordanova, V. K., Y. S. Miyoshi, S. Zaharia, M. F. Thomsen, G. D. Reeves, D. S. Evans, C. G. Mouikis, and J. F. Fennell (2006), Kinetic simulations of ring current evolution during the Geospace Environment Modeling challenge events, *J. Geophys. Res.*, *111*, A11S10, doi:10.1029/2006JA011644.

Jordanova, V. K., J. Albert, and Y. Miyoshi (2008), Relativistic electron precipitation by EMIC waves from self-consistent global simulations, *J. Geophys. Res.*, *113*, A00A10, doi:10.1029/2008JA013239.

Jordanova, V. K., H. Matsui, P. A. Puhl-Quinn, M. F. Thomsen, K. Mursula and L. Holappa (2009), Ring current development during high speed streams, *J. Atm. Sol. Terr. Phys.*, *71*, 1093–1102, doi:10.1016/j.jastp. 2008.09.043.

Jordanova, V. K., R. M. Thorne, W. Li, and Y. Miyoshi (2010a), Excitation of whistler mode chorus from global ring current simulations, *J. Geophys. Res.*, *115*, A00F10, doi:10.1029/2009JA014810.

Jordanova, V. K., S. Zaharia, and D. T. Welling (2010b), Comparative study of ring current development using empirical, dipolar, and self-consistent magnetic field simulations, *J. Geophys. Res.*, *115*, A00J11, doi:10.1029/2010JA015671.

Kennel, C. (1966), Low-frequency whistler mode, *Phys. Fluids*, *9*, 2190–2203.

Kennel, C. F., and H. Petschek (1966), Limit on stably trapped particle fluxes, *J. Geophys. Res.*, *71*, 1–28.

Kennel, C. F., and R. M. Thorne (1967), Unstable growth of unducted whistlers propagating at an angle to the geomagnetic field, *J. Geophys. Res.*, *72*, 871–878.

Kistler, L., F. Ipavich, D. Hamilton, G. Gloeckler, B. Wilken, G. Kremser, and W. Stüdemann (1989), Energy spectra of the major ion species in the ring current during geomagnetic storms, *J. Geophys. Res.*, *94*, 3579–3599.

Kozyra, J. U., et al. (2006), Response of the upper/middle atmosphere to coronal holes and powerful high-speed solar wind streams in 2003, in *Recurrent Magnetic Storms: Corotating Solar Wind Streams*, *Geophys. Monogr. Ser.*, vol. 167, edited by B. T. Tsurutani et al., pp. 319–340, AGU, Washington, D. C.

Krieger, A. S., A. F. Timothy, and E. C. Roelof (1973), A coronal hole and its identification as the source of a high velocity solar wind stream, *Sol. Phys.*, *29*, 505–525.

Lennartsson, W., E. G. Shelley, R. D. Sharp, R. G. Johnson, and H. Balsiger (1979), Some initial ISEE-1 results on the ring current composition and dynamics during the magnetic storm of December 11, 1977, *Geophys. Res. Lett.*, *6*, 483–486.

Li, W., R. M. Thorne, V. Angelopoulos, J. Bortnik, C. M. Cully, B. Ni, O. LeContel, A. Roux, U. Auster, and W. Magnes (2009), Global distribution of whistler-mode chorus waves observed on the THEMIS spacecraft, *Geophys. Res. Lett.*, *36*, L09104, doi:10.1029/2009GL037595.

Li, W., R. M. Thorne, J. Bortnik, Y. Nishimura, V. Angelopoulos, L. Chen, J. P. McFadden, and J. W. Bonnell (2010), Global distributions of suprathermal electrons observed on THEMIS and potential mechanisms for access into the plasmasphere, *J. Geophys. Res.*, *115*, A00J10, doi:10.1029/2010JA015687.

Li, X., M. Temerin, D. N. Baker, G. D. Reeves, and D. Larson (2001), Quantitative prediction of radiation belt electrons at geostationary orbit based on solar wind measurements, *Geophys. Res. Lett.*, *28*, 1887–1890.

Liu, K., S. P. Gary, and D. Winske (2011), Excitation of magnetosonic waves in the terrestrial magnetosphere: Particle-in-cell simulations, *J. Geophys. Res.*, *116*, A07212, doi:10.1029/2010JA016372.

Liu, S., M. W. Chen, J. L. Roeder, L. R. Lyons, and M. Schulz (2005), Relative contribution of electrons to the stormtime total ring current energy content, *Geophys. Res. Lett.*, *32*, L03110, doi:10.1029/2004GL021672.

Lorentzen, K. R., J. B. Blake, U. S. Inan, and J. Bortnik (2001), Observations of relativistic electron microbursts in association with VLF chorus, *J. Geophys. Res.*, *106*, 6017–6027.

Loto'aniu, T. M., B. J. Fraser, and C. L. Waters (2005), Propagation of electromagnetic ion cyclotron wave energy in the magnetosphere, *J. Geophys. Res.*, *110*, A07214, doi:10.1029/2004JA010816.

Mauk, B. H., and R. L. McPherron (1980), An experimental test of the electromagnetic ion cyclotron instability within the Earth's magnetosphere, *Phys. Fluids*, *23*(10), 2111–2127, doi:10.1063/1.862873.

Maynard, N. C., and A. J. Chen (1975), Isolated cold plasma regions: Observations and their relation to possible production mechanisms, *J. Geophys. Res.*, *80*, 1009–1013.

Meredith, N. P., R. B. Horne, and R. R. Anderson (2001), Substorm dependence of chorus amplitudes: Implications for the acceleration of electrons to relativistic energies, *J. Geophys. Res.*, *106*, 13,165–13,178, doi:10.1029/2000JA900156.

Meredith, N. P., R. M. Thorne, R. B. Horne, D. Summers, B. J. Fraser, and R. R. Anderson (2003), Statistical analysis of relativistic electron energies for cyclotron resonance with EMIC waves observed on CRRES, *J. Geophys. Res.*, *108*(A6), 1250, doi:10.1029/2002JA009700.

Meredith, N. P., R. B. Horne, and R. R. Anderson (2008), Survey of magnetosonic waves and proton ring distributions in the Earth's inner magnetosphere, *J. Geophys. Res.*, *113*, A06213, doi:10.1029/2007JA012975.

Meredith, N. P., R. B. Horne, M. M. Lam, M. H. Denton, J. E. Borovsky, and J. C. Green (2011), Energetic electron precipitation during high-speed solar wind stream driven storms, *J. Geophys. Res.*, *116*, A05223, doi:10.1029/2010JA016293.

Miyoshi, Y., and R. Kataoka (2008), Flux enhancement of the outer radiation belt electrons after the arrival of stream interaction regions, *J. Geophys. Res.*, *113*, A03S09, doi:10.1029/2007JA012506.

Mursula, K. (2007), Satellite observations of Pc1 pearl waves: The changing paradigm, *J. Atmos. Sol. Terr. Phys.*, *69*, 1623–1634, doi:10.1016/j.jastp.2007.02.013.

Nunn, D., A. Demekhov, V. Trakhtengerts, and M. J. Rycroft (2003), VLF emission triggering by a highly anisotropic electron plasma, *Ann. Geophys.*, *21*, 481–492.

Omura, Y., Y. Katoh, and D. Summers (2008), Theory and simulation of the generation of whistler-mode chorus, *J. Geophys. Res.*, *113*, A04223, doi:10.1029/2007JA012622.

Paulikas, G., and J. B. Blake (1979), Effects of the solar wind on magnetospheric dynamics: Energetic electrons at the synchronous orbit, in *Quantitative Modeling of Magnetospheric Processes*, *Geophys. Monogr. Ser.*, vol. 21, edited by W. P. Olsen, pp. 180–202, AGU, Washington, D. C.

Perraut, S., A. Roux, P. Robert, R. Gendrin, J. Sauvaud, J. Bosqued, G. Kremser, and A. Korth (1982), A systematic study of ULF waves above FH+ from GEOS 1 and 2 measurements and their relationships with proton ring distributions, *J. Geophys. Res.*, *87*, 6219–6236, doi:10.1029/JA087iA08p06219.

Rasmussen, C. E., S. M. Guiter, and S. G. Thomas (1993), Two-dimensional model of the plasmasphere: Refilling time constants, *Planet. Space Sci.*, *41*, 35–43.

Roederer, J. G. (1970), *Dynamics of Geomagnetically Trapped Radiation*, Springer, New York.

Russell, C. T., R. E. Holzer, and E. J. Smith (1970), OGO 3 observations of ELF noise in the magnetosphere: 2. The nature of the equatorial noise, *J. Geophys. Res.*, *75*, 755–768, doi:10.1029/JA075i004p00755.

Santolík, O., and D. A. Gurnett (2003), Transverse dimensions of chorus in the source region, *Geophys. Res. Lett.*, *30*(2), 1031, doi:10.1029/2002GL016178.

Santolík, O., J. S. Pickett, D. A. Gurnett, M. Maksimovic, and N. Cornilleau-Wehrlin (2002), Spatiotemporal variability and propagation of equatorial noise observed by Cluster, *J. Geophys. Res.*, *107*(A12), 1495, doi:10.1029/2001JA009159.

Sckopke, N. (1966), A general relation between the energy of trapped particles and the disturbance field over the Earth, *J. Geophys. Res.*, *71*, 3125–3130.

Sheeley, N. R., Jr., J. W. Harvey, and W. C. Feldman (1976), Coronal holes, solar wind streams and recurrent geomagnetic disturbances: 1973–1976, *Sol. Phys.*, *49*, 271–278.

Sibeck, D. G., R. W. McEntire, A. T. Y. Lui, R. E. Lopez, and S. M. Krimigis (1987), Magnetic field drift shell splitting: Cause of unusual dayside particle pitch angle distributions during storms and substorms, *J. Geophys. Res.*, *92*, 13,485–13,497.

Stern, D. P. (1975), The motion of a proton in the equatorial magnetosphere, *J. Geophys. Res.*, *80*, 595–599.

Summers, D., R. M. Thorne, and F. Xiao (1998), Relativistic theory of wave-particle resonant diffusion with application to electron acceleration in the magnetosphere, *J. Geophys. Res.*, *103*, 20,487–20,500.

Thorne, R. M., and R. B. Horne (1997), Modulation of electromagnetic ion cyclotron instability due to interaction with ring current O^+ during magnetic storms, *J. Geophys. Res.*, *102*, 14,155–14,163.

Thorne, R. M., and C. F. Kennel (1971), Relativistic electron precipitation during magnetic storm main phase, *J. Geophys. Res.*, *76*, 4446–4453.

Thorne, R. M., T. P. O'Brien, Y. Y. Shprits, D. Summers, and R. B. Horne (2005), Timescale for MeV electron microburst loss during geomagnetic storms, *J. Geophys. Res.*, *110*, A09202, doi:10.1029/2004JA010882.

Thorne, R. M., R. B. Horne, V. K. Jordanova, J. Bortnik, and S. A. Glauert (2006), Interaction of EMIC waves with thermal plasma and radiation belt particles, in *Magnetospheric ULF Waves: Synthesis and New Directions*, *Geophys. Monogr. Ser.*, vol. 169, edited by K. Takahashi et al., pp. 213–223, AGU, Washington, D. C.

Tsurutani, B. T., W. D. Gonzalez, A. L. C. Gonzalez, F. Tang, J. K. Arballo, and M. Okada (1995), Interplanetary origin of geomagnetic activity in the declining phase of the solar cycle, *J. Geophys. Res.*, *100*, 21,717–21,733.

Tsyganenko, N. A., and M. I. Sitnov (2005), Modeling the dynamics of the inner magnetosphere during strong geomagnetic storms, *J. Geophys. Res.*, *110*, A03208, doi:10.1029/2004JA010798.

Turner, N. E., D. N. Baker, T. I. Pulkkinen, and R. L. McPherron (2000), Evaluation of the tail current contribution to *Dst*, *J. Geophys. Res.*, *105*, 5431–5439.

Turner, N. E., E. J. Mitchell, D. J. Knipp, B. A. Emery, (2006), Energetics of magnetic storms driven by corotating interaction regions: A study of geoeffectiveness, in *Recurrent Magnetic Storms: Corotating Solar Wind Streams*, *Geophys. Monogr. Ser.*, vol. 167, edited by B. T. Tsurutani et al., pp. 113–124, AGU, Washington, D. C.

Volland, H. (1973), A semiempirical model of large-scale magnetospheric electric fields, *J. Geophys. Res.*, *78*, 171–180.

Weimer, D. R. (2001), An improved model of ionospheric electric potentials including substorm perturbations and application to the Geospace Environment Modeling November 24, 1996, event, *J. Geophys. Res.*, *106*, 407–416.

Welling, D. T., V. K. Jordanova, S. Zaharia, A. Glocer, and G. Toth (2011), The effects of dynamic ionospheric outflow on the ring current, *J. Geophys. Res.*, *116*, A00J19, doi:10.1029/2010JA015642.

Wrenn, G. L. (2009), Chronology of "killer" electrons: solar cycles 22 and 23, *J. Atmos. Sol. Terr. Phys.*, *71*, 1210–1218, doi:10.1016/j.jastp.2008.08.002.

Young, D., H. Balsiger, and J. Geiss (1982), Correlations of magnetospheric ion composition with geomagnetic and solar activity, *J. Geophys. Res.*, *87*, 9077–9096.

Yu, Y., V. Jordanova, S. Zaharia, J. Koller, J. Zhang, L. M. Kistler (2012), Validation study of the magnetically self-consistent inner magnetosphere model RAM-SCB, *J. Geophys. Res.*, *117*, A03222, doi:10.1029/2011JA017321.

Zaharia, S. (2008), Improved Euler potential method for three-dimensional magnetospheric equilibrium, *J. Geophys. Res.*, *113*, A08221, doi:10.1029/2008JA013325.

Zaharia, S., and C. Z. Cheng (2003), Near-Earth thin current sheets and Birkeland currents during substorm growth phase, *Geophys. Res. Lett.*, *30*(17), 1883, doi:10.1029/2003GL017456.

Zaharia, S., C. Z. Cheng, and K. Maezawa (2004), 3-D force-balanced magnetospheric configurations, *Ann. Geophys.*, *22*, 251–265, doi:1432-0576/ag/2004-22-251.

Zaharia, S., V. K. Jordanova, M. F. Thomsen, and G. D. Reeves (2006), Self-consistent modeling of magnetic fields and plasmas in the inner magnetosphere: Application to a geomagnetic storm, *J. Geophys. Res.*, *111*, A11S14, doi:10.1029/2006JA011619.

Zaharia, S., V. K. Jordanova, D. T. Welling, and G. Toth (2010), Self-consistent inner magnetosphere simulation driven by a global MHD model, *J. Geophys. Res.*, *115*, A12228, doi:10.1029/2010JA015915.